

Spectroscopic follow-up of a cluster candidate at $z = 1.45$

Caroline van Breukelen,^{1*} Garret Cotter,¹ Steve Rawlings,¹ Tony Readhead,²
David Bonfield,¹ Lee Clewley,¹ Rob Ivison,^{3,4} Matt Jarvis,⁵ Chris Simpson⁶
and Mike Watson⁷

¹*Astrophysics, Department of Physics, Keble Road, Oxford OX1 3RH*

²*Owens Valley Radio Observatory, California Institute of Technology, Pasadena, CA 91125, USA*

³*UK Astronomy Technology Centre, Royal Observatory, Blackford Hill, Edinburgh EH9 3HJ*

⁴*Scottish Universities Physics Alliance, Institute for Astronomy, University of Edinburgh, Blackford Hill, Edinburgh EH9 3HJ*

⁵*Centre for Astrophysics, Science & Technology Research Institute, University of Hertfordshire, Hatfield AL10 9AB*

⁶*Astrophysics Research Institute, Liverpool John Moores University, Twelve Quays House, Egerton Wharf, Birkenhead CH41 1LD*

⁷*X-ray Astronomy Group, Department of Physics and Astronomy, University of Leicester, Leicester LE1 7RH*

Accepted 2007 August 29. Received 2007 August 28; in original form 2007 July 23

ABSTRACT

We have obtained deep optical spectroscopic data of the highest-redshift cluster candidate ($z \sim 1.4$, CVB13) selected by Van Breukelen et al. in a photometric optical/infrared catalogue of the Subaru *XMM–Newton* Deep Field. The data, which comprise 104 targeted galaxies, were taken with the DEep Imaging Multi-Object Spectrograph on the Keck 2 telescope and yielded 31 secure redshifts in the range $1.25 < z < 1.54$ within a 7×4 -arcmin² field centred on CVB13. Instead of one massive cluster at $z = 1.4$, we find evidence for three projected structures at $z = 1.40, 1.45$ and 1.48 . The most statistically robust of these structures, at $z = 1.454$, has six spectroscopically confirmed galaxies. Its total mass is estimated at $\gtrsim 10^{14} M_{\odot}$ and it may therefore be termed a cluster. There is an X-ray source at the cluster position which is marginally spatially resolved but whose X-ray spectrum is too hard to be thermal cluster emission. Its origin could be the summed X-ray emission from active galaxies in, and projected on to, the cluster. Serendipitously, we have discovered a cluster at $z = 1.28$ with a mass of $\gtrsim 10^{14} M_{\odot}$ at the same position on the sky, comprising six spectroscopically confirmed cluster galaxies and at least one additional radio source. The selection of CVB13 for the cluster catalogue was evidently aided by the superposition of other, presumably lower mass, structures, whereas the single cluster at $z = 1.28$ contained too few galaxies to be isolated by the same algorithm. Given the complicated nature of such structures, caution must be employed when measuring the mass function of putative high-redshift clusters with photometric techniques alone.

Key words: galaxies: clusters: general – galaxies: high-redshift – radio continuum: general – X-rays: galaxies – X-rays: galaxies: clusters.

1 INTRODUCTION

Clusters of galaxies are important probes for both cosmology and astrophysics. They are the most-massive virialized structures in the Universe, and they are therefore excellent targets to study large-scale structure formation. The cluster mass function directly links to the normalization of the power spectrum of density perturbations, σ_8 , which is the rms in the density on a scale of $8 h^{-1} \text{Mpc}$ ($h = H_0/100 \text{ km s}^{-1} \text{Mpc}^{-1}$). The evolution of the mass function

with redshift reflects the growth function of the Universe, which is determined by Ω_M (the matter density parameter), Ω_{Λ} (the dark energy density parameter), and w (the dark energy equation-of-state parameter). Further, clusters are of great interest to astrophysics because they can be approximated by a ‘closed-box’ environment. This makes them ideal laboratories to study the interaction of galaxies and the intergalactic medium, which is thought to play a large role in galaxy formation and evolution. An important remaining question is why so little baryonic matter in clusters forms stars (e.g. Cole 1991; White & Frenk 1991). Feedback processes coupling baryonic matter from galaxies to the intergalactic medium are likely to counter further condensation of the intergalactic gas and halt star formation. Two examples of these processes are galactic winds due to multiple

*E-mail: cvb@astro.ox.ac.uk

†Now at: NASA Goddard Space Flight Center, Greenbelt, MD 20771, USA.

supernovae in starburst galaxies (e.g. Heckman 2002) and outflow from radio-loud active galactic nuclei (AGN) (e.g. Scannapieco & Oh 2004; Fabian, Celotti & Erlund 2006a).

Cluster searches have been carried out for decades. The first extensive cluster catalogue was created by Abell (Abell 1958; Abell, Corwin & Olowin 1989). Unfortunately, Abell only had single-filter photographic plates at his disposal and therefore his work was severely complicated by projection effects. Gladders et al. (1998) improved on this situation by showing that a redshift estimate can be determined by using only two filters and targeting the bright, red elliptical galaxy population in clusters which form the red sequence (e.g. Bower, Lucey & Ellis 1992). A particularly important advance in optical cluster detection has come from the advent of large arrays of CCD detectors allowing large surveys to be carried out efficiently, such as the relatively shallow ($z < 0.4$) but very wide field Sloan Digital Sky Survey (SDSS) (e.g. Goto et al. 2002; Kim et al. 2002; Miller et al. 2005). There have been numerous smaller area surveys to higher redshifts, for example, the Palomar Distant Cluster Survey (Postman et al. 1996), the ESO Imaging Survey (Lobo et al. 2000), and the Red Sequence Cluster Survey (Gladders & Yee 2005). Moving to even higher redshifts, protoclusters have been found by focusing on fields around quasars or radio galaxies (e.g. Venemans et al. 2002) as a large fraction of these objects have been shown to reside in clusters (see Pascarelle et al. 1996; Röttgering et al. 1996). However, selecting clusters in blank sky surveys with optical photometry at redshifts $z \gtrsim 1$ was impractical for a long time because of the shifting of the 4000-Å break – characteristic for the red, passively evolving ellipticals predominantly found in clusters – out of the *I* band to longer wavelength bands.

The launch of the *ROSAT* satellite in 1990 greatly advanced the study of clusters in the X-ray regime, enabling the discovery of hundreds of clusters up to $z \sim 1$. Later *Chandra* and *XMM-Newton* provided the possibility to observe even deeper owing to their unprecedented sensitivity and angular resolution. X-ray cluster surveys now extend well above $z \sim 1$ (e.g. Stanford et al. 2001; Rosati et al. 2004; Bremer et al. 2006). Stanford et al. (2006) currently hold the record of the most-distant spectroscopically confirmed cluster at $z = 1.451$. This cluster was initially detected as an extended source in *XMM* X-ray data; spectroscopic follow-up revealed five cluster galaxies within a 1 arcmin diameter. The temperature of the intra-cluster medium (ICM) was shown to be ~ 7 keV, which is the highest detected in any cluster at $z > 1$, implying a relatively massive cluster for such a high redshift.

Another way to observe the ICM is through the Sunyaev-Zeldovich effect (S-Z effect, Sunyaev & Zeldovich 1970, 1972). This effect is visible as a distortion of the cosmic microwave background (CMB): as the CMB photons travel through the ICM they are subjected to inverse Compton scattering, which shifts the energies of a small fraction of the photons slightly upwards. In the last decade, many detections have been made of the S-Z effect (e.g. Birkinshaw 1999; Carlstrom et al. 2000; Jones et al. 2005) and comprehensive S-Z surveys are underway (Kneissl et al. 2001). Cotter et al. (2002) used pointed S-Z observations to detect hot gas associated with a $z \sim 1$ cluster of radio sources.

Recent developments of wide-field infrared cameras, such as the Wide-Field CAMera (WFCAM) on the United Kingdom InfraRed Telescope (UKIRT), have brought photometric cluster surveys back into vogue by enabling deep, large-scale infrared surveys and pushing the limit of photometric cluster selection to significantly higher redshifts. The UKIRT Infrared Deep Sky Survey (UKIDSS, Lawrence et al. 2007) is a suite of both wide and deep infrared imaging surveys using WFCAM. The Ultra Deep Survey is the deepest

of these, and covers 0.8 deg^2 in the Subaru *XMM-Newton* Deep Field (SXDF, Sekiguchi et al., in preparation) with a planned limiting magnitude of $K_{\text{vega}} = 23$. Deep *BVRi'z'* imaging data from the Subaru Telescope are also available on the SXDF (Furusawa et al., in preparation), as are X-ray data by *XMM-Newton* (Watson et al. 2004), radio data from the Very Large Array (Simpson et al. 2006; Ivison et al. 2007), and *Spitzer* infrared data ranging from 3.6 to 24 μm (Lonsdale et al. 2005).

We previously exploited these exceptional multiwavelength data sets to execute a high-redshift cluster survey, using photometric redshifts, as reported in Van Breukelen et al. (2006) (VB06). In VB06, we isolated 13 cluster candidates at $0.6 < z < 1.4$ in 0.5 deg^2 of the SXDF. The highest-redshift cluster candidate, CVB13 [RA = $02^{\text{h}}18^{\text{m}}10^{\text{s}}.5$, Dec. = $-05^{\circ}01'05''$ (J2000)], was estimated to lie at $z = 1.39 \pm 0.07$.

In this paper, we present the spectroscopic follow-up of the putative CVB13 cluster with the DEep Imaging Multi-Object Spectrograph (DEIMOS, Cowley et al. 1997) on the 10-m Keck 2 telescope. Section 2 describes the observations and data reduction. The analysis and discussion on the nature of the system are given in Section 3. Section 4 contains concluding remarks. Throughout this paper, we use $H_0 = 70 \text{ km s}^{-1} \text{ Mpc}^{-1}$ ($h = 0.7$), $\Omega_{\text{M}} = 0.3$ and $\Omega_{\Lambda} = 0.7$ and a Λ cold dark matter power spectrum with $\sigma_8 = 0.75$; all sky coordinates are quoted in equinox J2000.

2 THE DATA

2.1 Selection of the targets

We selected four samples of target galaxies to create a Multi-Object Spectroscopy (MOS) mask. Each of these samples comprised groups of different priorities. The samples are described below; the masks were created by allocating the maximum number of slits to sample 1, priority 1, and moving down through all the priorities within the sample before allocating slits to the next sample.

(i) *Sample 1*. This sample included all galaxies that were determined to be a possible cluster member of CVB13 by the algorithm described in VB06. The algorithm presented in this paper used two methods to detect clusters: Voronoi Tessellations and Friends-of-Friends. The galaxies that were assigned to the cluster by both methods composed the highest-priority target group within this sample. The second priority group comprised the cluster members as selected only by Friends-of-Friends, followed by the galaxies found only by Voronoi Tessellations, as this is a less-reliable method to determine cluster membership (see VB06). The target list of this sample consisted of a total of 125 objects, of which 18 objects are of priority 1, three are of priority 2, and 104 are of priority 3. Slits could be placed on 61 out of these 125 targets, divided into priorities: priority 1 – 10 galaxies, priority 2 – 0 galaxies and priority 3 – 51 galaxies.

(ii) *Sample 2*. By rotating the DEIMOS instrument by 90° , we were able to utilize the long axis of the field of view to target another candidate cluster from VB06 within the same observations. This was cluster 6 (CVB6) at $z = 0.76 \pm 0.12$, RA = $02^{\text{h}}18^{\text{m}}32^{\text{s}}.7$, Dec. = $-05^{\circ}01'04''$. The target galaxies for this sample were selected and prioritized exactly as done for sample 1. There were 152 targets in total, divided into priorities: priority 1 – 30, priority 2 – 1 and priority 3 – 121. Out of these, 64 sources could be observed: 13 of priority 1, one of priority 2, and 50 of priority 3.

(iii) *Sample 3*. The third sample consisted of various active galaxies in the field, detected by their X-ray activity, radio emission, or

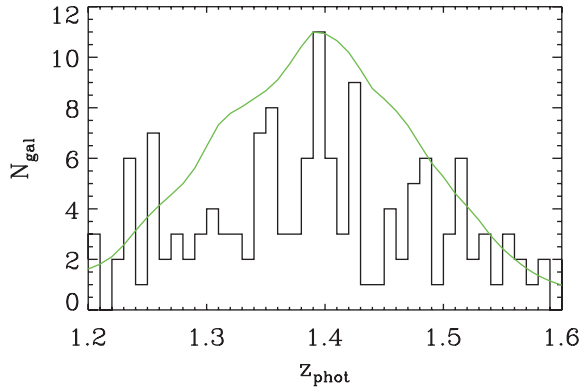


Figure 1. Histogram of the photometric redshifts of galaxies in the field of CVB13 ($02^{\text{h}}17^{\text{m}}54^{\text{s}}.6 \leq \text{RA} \leq 02^{\text{h}}18^{\text{m}}26^{\text{s}}.4$ and $-05^{\circ}03'05'' \leq \text{Dec.} \leq -04^{\circ}59'05''$ in the redshift range $1.2 < z < 1.6$). At $z = 1.4$, the projected region of interest has a proper size $3.6 \times 2.0 \text{ Mpc}^2$. The photometric redshifts were calculated using Bruzual & Charlot (2003) modelled spectral energy distributions from stellar population synthesis (see VB06 for a discussion of the photometric redshifts). The solid line is the sum of the redshift probability functions (normalized to the peak of the histogram) of the galaxies with a photometric redshift within the shown redshift range.

excess flux in the *Spitzer* 24- μm band. We found 48 radio sources in the field, which made up priority group 1. The second priority group included 31 X-ray sources. The last priority group consisted of 12 objects with a detection in the 24- μm band and a colour of $J - K = 2$. The target list comprised 91 sources, out of which 26 were observed (15 radio sources, eight X-ray sources and three 24- μm sources).

(iv) *Sample 4.* The final sample was designed to fill up all remaining slits in the two masks. It included all galaxies in the field with a photometric redshift of $1.25 < z_{\text{phot}} < 1.54$. Fig. 1 is a histogram of the photometric redshifts of these objects; overplotted is the sum of their redshift probability distribution functions. The chosen redshift range corresponds to the $\pm 2\sigma$ range on the photometric redshift of the cluster candidate CVB13. This error on the cluster redshift reflects the combined redshift probability distribution functions of the cluster candidate members as given in VB06. This sample consisted of 1139 objects out of which 43 were observed.

2.2 Observations and data reduction

Optical spectroscopy was undertaken on the 2006 December 21 using the DEIMOS instrument on the Keck 2 telescope. The telescope was pointed at $\text{RA} = 02^{\text{h}}18^{\text{m}}20^{\text{s}}.00$, $\text{Dec.} = -05^{\circ}01'04''.9$ and the field of view of the instrument, with a position angle of 90° , was $16.7 \times 5 \text{ arcmin}^2$ in $\text{RA} \times \text{Dec.}$ The two MOS masks comprised 1-arcsec-wide slits. The 600 line mm^{-1} grating was used in conjunction with the GG495 order-blocking filter. A long-slit observation of Feige 110 was taken for spectrophotometric calibration. Four 1800-s integrations were taken for each mask, and short-exposure images were taken through the mask after each spectroscopic integration to ensure mask alignment. Seeing, as measured on the alignment images, varied between 0.6 and 1.0 arcsec. Conditions were photometric throughout.

The two-dimensional spectra were reduced with the DEEP2 DEIMOS Data Pipeline.¹ The pipeline processes the flats and arcs to determine the position of the slitlets on the CCD and to find the

two-dimensional wavelength solution for each slitlet. Subsequently, the spectra are flat-field corrected and the curvature of the spectra in the spatial direction is rectified. The separate science exposures are sky-subtracted and finally combined into one mean, cosmic-ray-rejected, science frame.

We extracted the one-dimensional spectra with a boxcar extraction routine, using a 0.8-arcsec-width aperture. To enable flux calibration, the standard star long-slit exposure was reduced with the IRAF package ‘TWOSSPEC’. The sensitivity function was determined using the IRAF task ‘SENSFUNC’ and the one-dimensional science spectra were calibrated with the task ‘CALIBRATE’. We note that for the average seeing of 0.8 arcsec we missed ~ 13 per cent of a typical galaxy’s flux within our aperture.

2.3 The spectroscopic sample

Overall the two MOS masks targeted 194 objects. Out of these, we were able to assign redshifts to 139 galaxies (72 per cent), which were divided over the samples as follows: 38 redshifts in sample 1, 57 redshifts in sample 2, 23 redshifts in sample 3, and 21 redshifts in sample 4. The remaining 28 per cent of the observed galaxies had continua too faint to allow a redshift determination from absorption features and showed no emission lines. Fig. 2 shows the positions of the targets within the DEIMOS field of view where each sample is depicted in a different colour.

In this paper, we focus solely on the cluster candidate CVB13. We therefore imposed two selection criteria to create our final spectroscopic sample: (i) the objects had to be within the $7 \times 4\text{-arcmin}^2$ field centred on $\text{RA} = 02^{\text{h}}18^{\text{m}}10^{\text{s}}.5$ and $\text{Dec.} = -05^{\circ}01'05''$ (see the Fig. 1 caption for RA and Dec. limits of the sample); and (ii) the redshift range was restricted to $1.25 < z < 1.54$, which was the original 2σ range of cluster candidate redshift (see Section 2.1). There were 30 objects in our DEIMOS data that satisfied these criteria, out of which 25 were from target sample 1 and five from target sample 4. These objects are shown in Fig. 2 with the red circles. We added one galaxy to our final sample that was observed with the Gemini Multi-Object Spectrograph (GMOS, Hook et al. 2004) on the Gemini North Telescope in Hawaii and satisfied the same selection criteria. The respective sample selection and data description can be found in Van Breukelen et al. (in preparation). This brought the total of the final spectroscopic sample to 31 objects.

3 ANALYSIS AND DISCUSSION

3.1 Properties of the line emitters

Due to the high redshift of our spectroscopic sample of 31 galaxies, the continua of the spectra are weak, rendering redshift determination by absorption features alone unfeasible. All redshifts in the final sample were therefore calculated from the [O II] emission line at 3727 Å. The identification of the [O II] line is reliable because in some cases the doublet was resolved, in others there were supporting absorption features, or there were no other emission lines visible within the spectral range that would be expected if the [O II] line was actually another emission line at a different redshift. The one- and two-dimensional spectra of the detected emission lines are shown in Fig. 3, where the identified line features are labelled and noisy sky regions are shaded. The three-dimensional distribution of the galaxies within our target area is depicted in Fig. 4 in comoving coordinates (X corresponds to RA, Y to Dec. and z to redshift). The galaxies are colour-coded to redshift, from blue at $z = 1.25$ to red at $z = 1.53$.

¹ <http://astro.berkeley.edu/~cooper/deep/spec2d/>

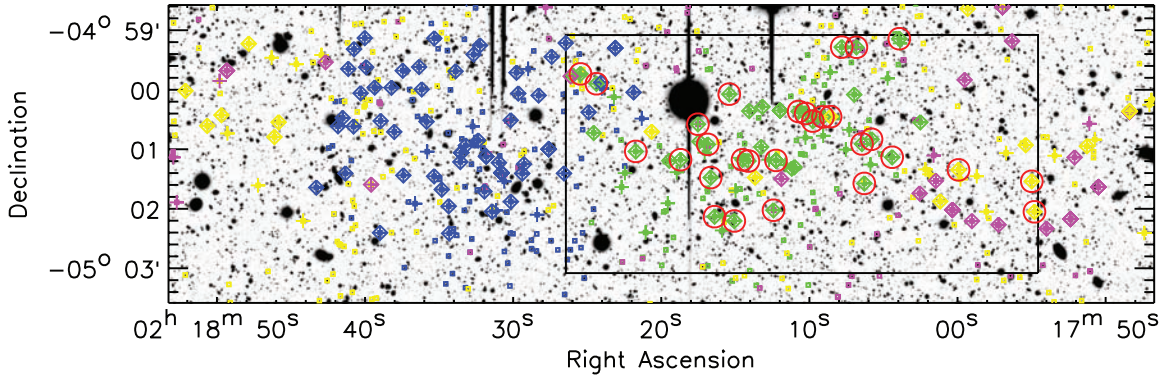


Figure 2. Spectroscopy targets overlaid on the i' -band image (Furusawa et al., in preparation) of the DEIMOS field of view. Sample 1 is depicted in the green symbols, sample 2 in the blue, sample 3 in the purple, and sample 4 in the yellow symbols (see Section 2.1). The small squares symbolize all the objects in the target list, the pluses are the objects that were actually observed, and the diamonds are all the targets for which a redshift could be determined. The red circles are the objects which are included in the final spectroscopic sample for this paper: they fall within the depicted box of 7×4 arcmin² centred on RA = $02^{\text{h}}18^{\text{m}}10^{\text{s}}$, Dec. = $-05^{\circ}01'05''$ and have redshifts of $1.25 < z < 1.54$ (see Section 2.3).

To determine the exact redshift, the line flux and the equivalent width of the [O II] emitters, we fit a line profile to the [O II] emission line in each object. As the [O II]₃₇₂₇ line is a doublet, the fitted line profile consists of two Gaussians at $\lambda_{\text{rest}} = 3726.1$ and 3728.8 \AA . The full width at half-maximum (FWHM) of each Gaussian is assumed to be equal, and is a free parameter of the fitted function. The other parameters are the redshift, the continuum level, and the ratio of fluxes of the two lines. The flux ratio is constrained to be within the limits for high and low density (Osterbrock 1967), corresponding to $0.35 \leq F_{3729}/F_{3726} \leq 1.5$, where F is the single line flux. Random errors on the flux and redshift measurements are determined by fitting modelled lines with the same procedure.

We calculate the star formation rate (SFR) of the galaxies using the equation given by Kennicutt (1998):

$$\text{SFR} = (1.4 \pm 0.4) \times 10^{-34} L_{[\text{O II}]}, \quad (1)$$

where the SFR is in $M_{\odot} \text{ yr}^{-1}$ and $L_{[\text{O II}]}$ is the luminosity of the [O II]₃₇₂₇ emission line in Watts. This equation assumes $L_{[\text{O II}]} / L_{\text{H}\alpha} = 0.57$ and a Salpeter initial mass function (IMF) with stellar masses between 0.1 and $100 M_{\odot}$. Extinction or total obscuration is not corrected for and therefore these estimates represent lower limits on the SFR. The properties of the complete sample can be found in Table 1. In this table, the redshift has been converted to heliocentric redshift (see Danese, de Zotti & di Tullio 1980).

3.2 Sample completeness

To estimate the completeness of our spectroscopic sample, we have to take the following three factors into account.

(i) The original target list was compiled from the UKIDSS-UDS Early Data Release (EDR) catalogue, which has a limiting K -band magnitude of $K_{\text{Vega}} = 20.6$. Cirasuolo et al. (2007) present a K -band luminosity function of galaxies in the UKIDSS-UDS in different redshift bins. We can calculate the total expected number of galaxies using their Schechter function for the redshift range $1.25 < z < 1.50$, characterized by $\phi^* = 2.6 \pm 0.3 \times 10^{-3} \text{ Mpc}^{-3}$, $M_{K, \text{Vega}}^* = -24.93 \pm 0.16$, and $\alpha = -0.92 \pm 0.18$. In our field of 7×4 arcmin² and $1.25 < z < 1.54$, we would expect 391 galaxies in total; when we impose the magnitude limit of $K_{\text{Vega}} = 20.6$, we would only expect to detect 99 objects, or 25 per cent.

(ii) The nature of an MOS mask makes complete sampling of the target list impossible. Out of our original target list, 177 objects

satisfied our selection criteria (see Section 2.1), using photometric redshifts for the redshift criterion of $1.25 < z < 1.54$. Of these objects, 75 were observed with the MOS masks. This means our spectroscopic data sampled 42 per cent of the galaxies we intended to target.

(iii) All the objects in our sample are [O II] emitters. We only detect the [O II] lines with a line flux $> 1.0 \times 10^{34} \text{ W m}^{-2}$. Furthermore, sky lines raise the flux limit of the [O II] line that we can detect in specific parts of the spectra. However, this affects lines with different linewidths in different ways. We determine our detection completeness of [O II] lines with a flux greater than the flux limit of $1.0 \times 10^{34} \text{ W m}^{-2}$ by modelling a two-dimensional [O II]₃₇₂₇ line. The modelled lines have a rest-frame FWHM varying between 1.3 and 7.6 \AA and fluxes from 10^{-20} to $10^{-19} \text{ W m}^{-2}$, corresponding to the range of observed rest-frame FWHMs and line fluxes. We add the modelled lines at redshifts of $1.25 \leq z \leq 1.54$ to a two-dimensional sky frame and try to recover the lines with the same procedure as used for the real spectra. Assuming a uniform distribution over the FWHM range and a Schechter distribution in flux, we calculate the fraction of missed sources at each redshift bin to find the detection completeness of [O II] lines with flux $> 1.0 \times 10^{34} \text{ W m}^{-2}$. The result ranges from 22 per cent at the locations of the strongest sky lines up to 97 per cent at the regions of the spectra with the least sky background noise.

Fig. 5 (left-hand panel) shows the redshift distribution of the 31 objects in our sample. Overplotted on the spectroscopic redshift histogram is the expected number of [O II] emitters per redshift bin in our field, calculated with the observed Schechter luminosity function for [O II] emitters at $z = 1.47$ from Ly et al. (2007): $\log_{10}(\phi^*/\text{Mpc}^{-3}) = -1.97 \pm 0.06$; $\log_{10}(L^*/W) = 35.60 \pm 0.05$; $\alpha = -0.78 \pm 0.13$. The expected number of [O II] emitters is corrected by multiplying by the wavelength-dependent product of the three completeness factors, namely $0.25 \times 0.42 \times (0.22-0.97)$. Note that this implicitly assumes no correlation between [O II] flux and the observed K -band magnitude. However, if, for example, the rest-frame equivalent width of the [O II] line is constant with the absolute blue magnitude of the galaxies, we would expect a positive correlation between [O II] flux and the rest-frame blue magnitude. Therefore, if the colours of the [O II] emitters are constant, we would expect a positive correlation between [O II] flux and the observed K -band magnitude. This would make the completeness factor of 0.25 in point (i) an underestimate. On the other hand, if the colour

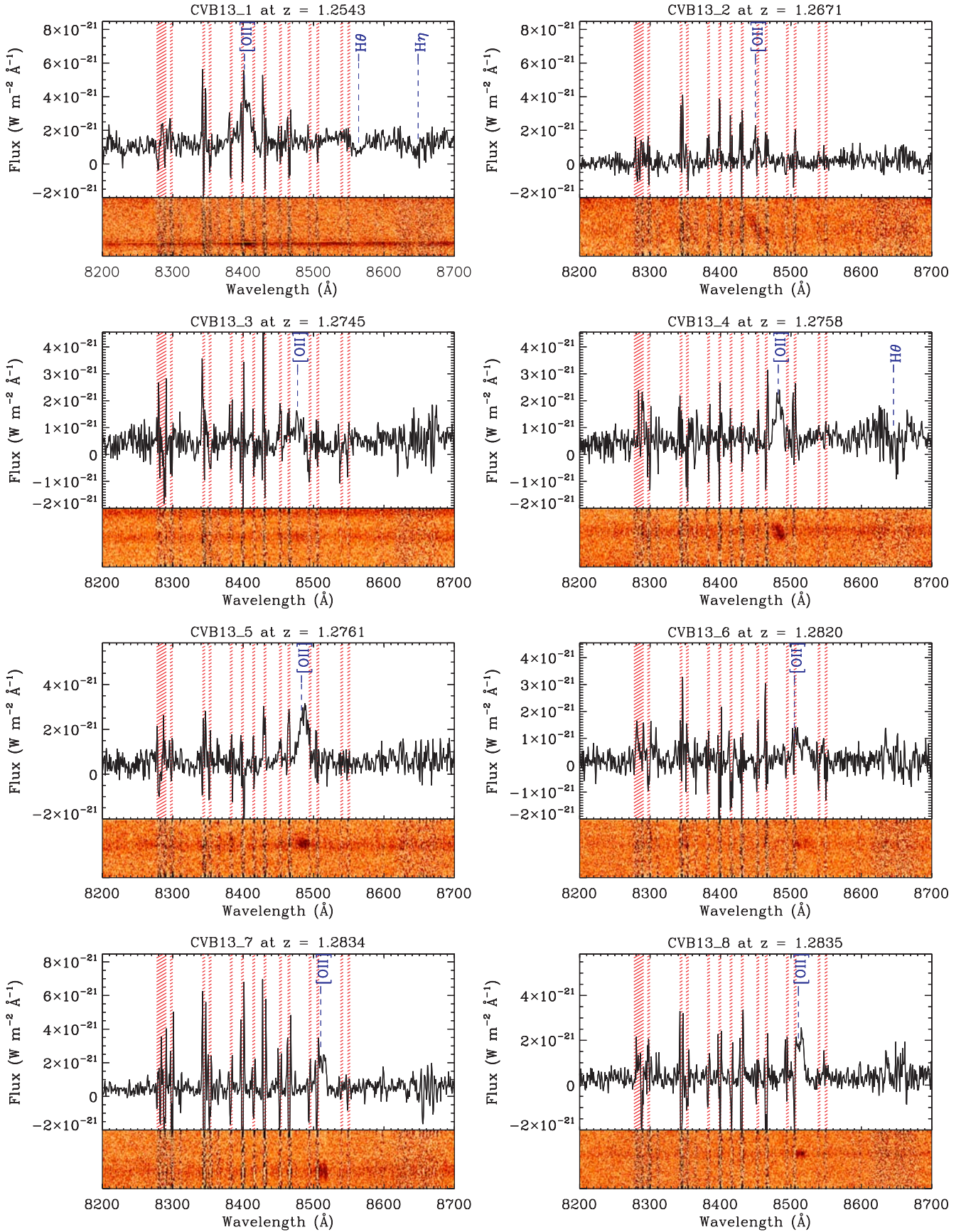


Figure 3. One-dimensional and two-dimensional DEIMOS spectra of the galaxies in the field of CVB13. Identified emission and absorption features are labelled. The shaded regions denote noisy parts of the spectra due to sky lines.

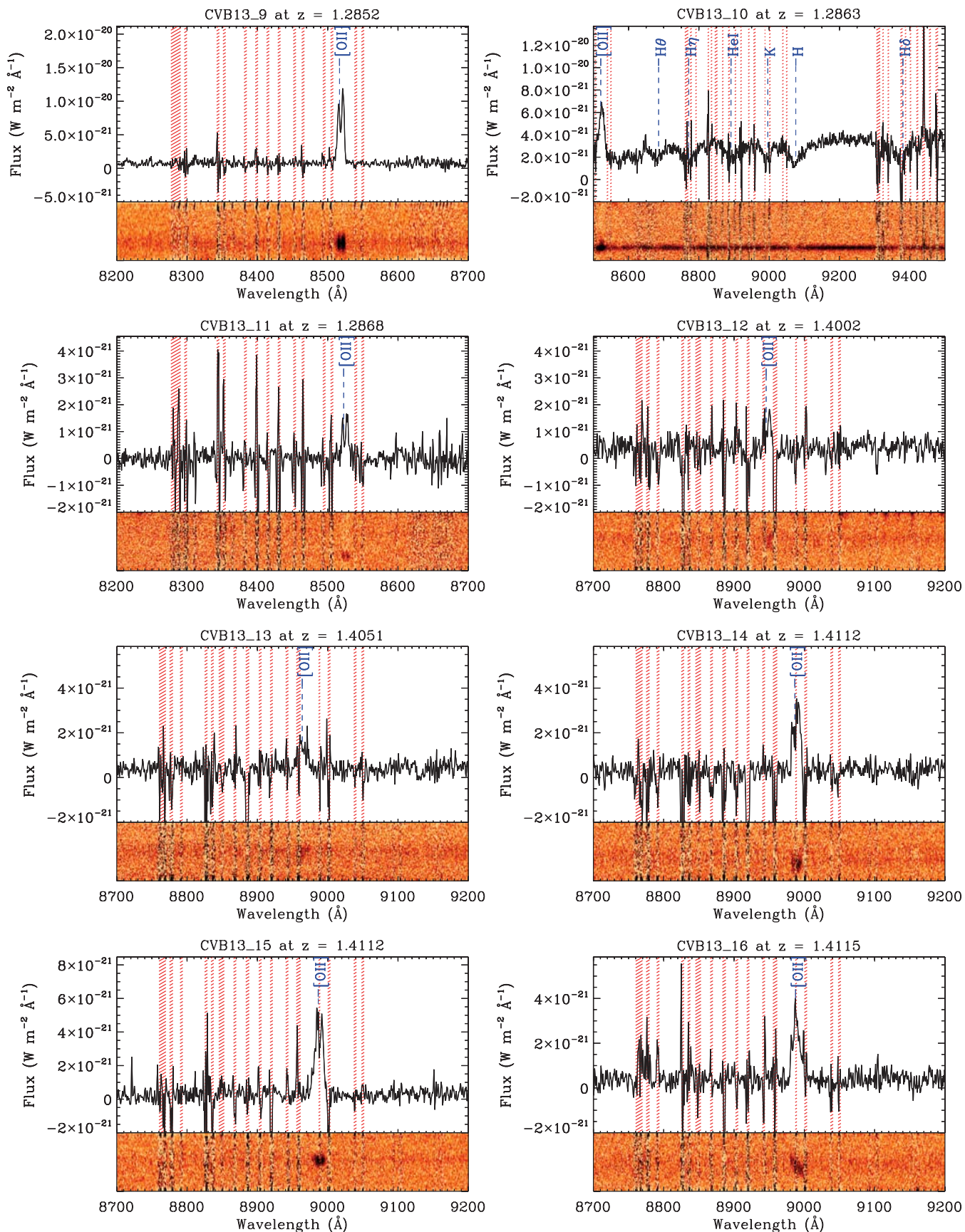


Figure 3 – continued

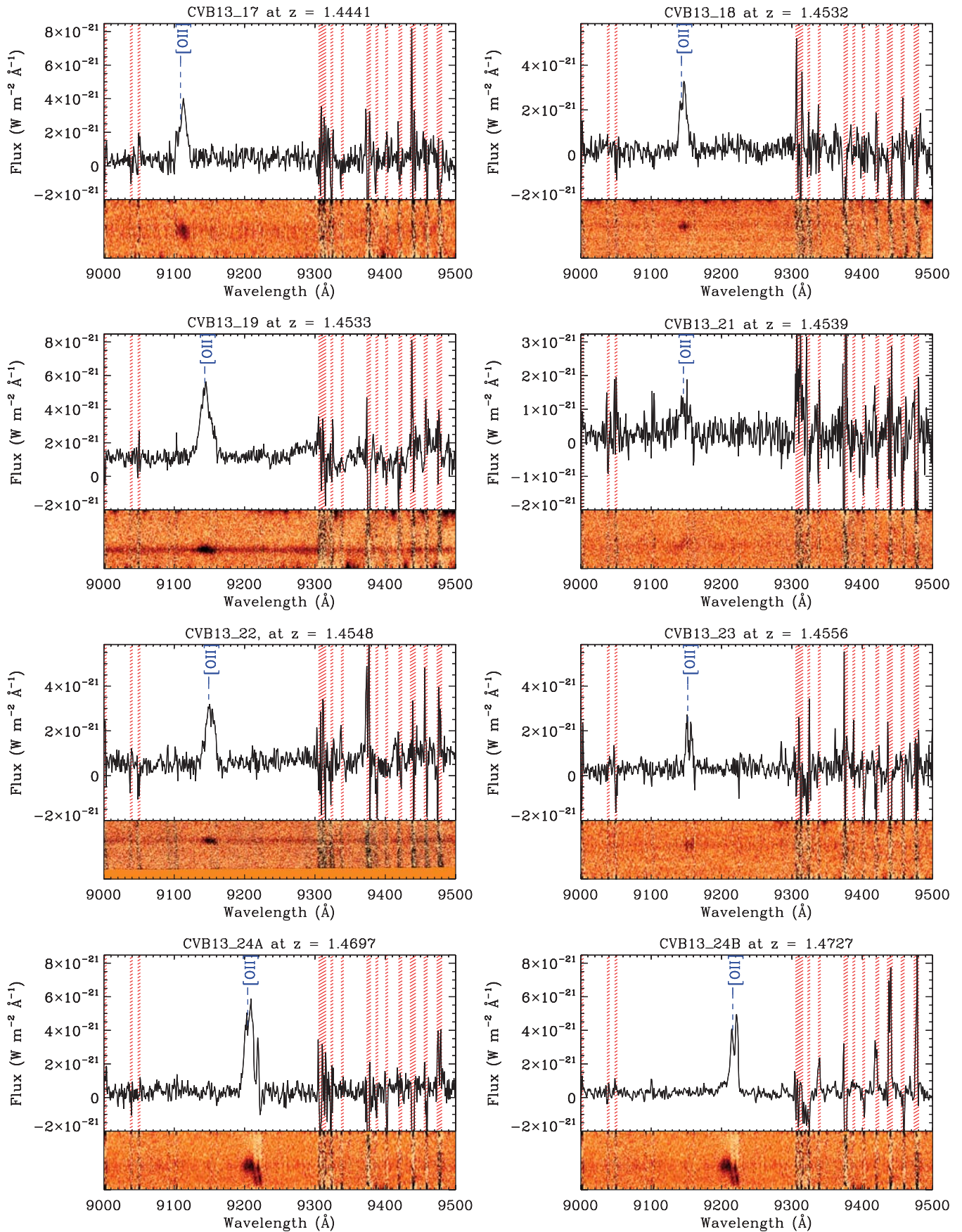


Figure 3 – continued

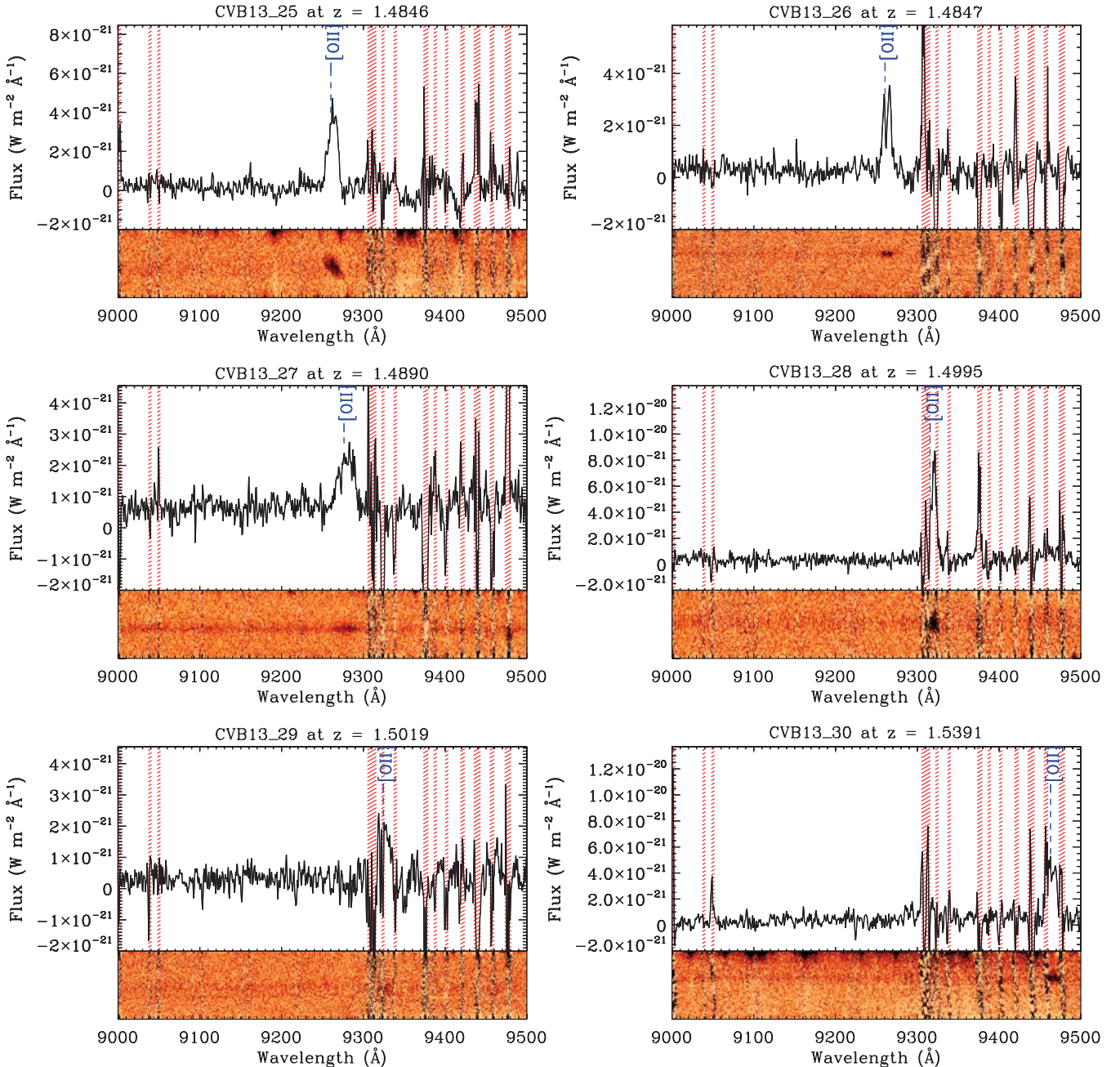


Figure 3 – continued

term is bluer for galaxies with a higher SFR – and hence brighter [O II] emission – then this would counter the positive correlation. Studies of [O II] emission at $z \sim 0-1$ (e.g. Hogg et al. 1998) do not allow us to separate these effects, so we adopt the 0.25 completeness factor and discuss the effects of extreme departures from this value in Section 3.3.

3.3 Evidence of clustering

The distribution of photometric redshifts in the field of CVB13 has a clear peak at $z = 1.4$, as is shown in Fig. 1. Spectroscopic follow-up, however, shows that the single redshift peak at $z = 1.4$ separates into three less-significant peaks at $z = 1.40$, 1.45 and 1.48 , as pictured in Fig. 5 (left-hand panel). There is also a clear overden-

sity at $z = 1.28$ which was not detected in the photometric redshift catalogue.

Following the method of Brand et al. (2003), we calculate the probability in each redshift bin (using Poissonian low-number statistics) that the number of [O II] emitters is greater than the number detected, given the number of [O II] emitters predicted by the model. The result is shown in Fig. 5 (right-hand panel) for bin sizes of $\Delta z = 0.0025$ (120 bins, black solid line), $\Delta z = 0.005$ (60 bins, blue dotted line), and $\Delta z = 0.01$ (30 bins, red dashed line). For a bin size of $\Delta z = 0.01$, the redshift peaks at $z = 1.28$ and 1.45 both have a probability of 10^{-5} . As there are 30 bins with this bin size, one would expect to find such a low value in 0.03 per cent drawn from a set of random realizations. Based on these statistics, we deem the structures at $z = 1.28$ and 1.45 to be highly significant overdensities.

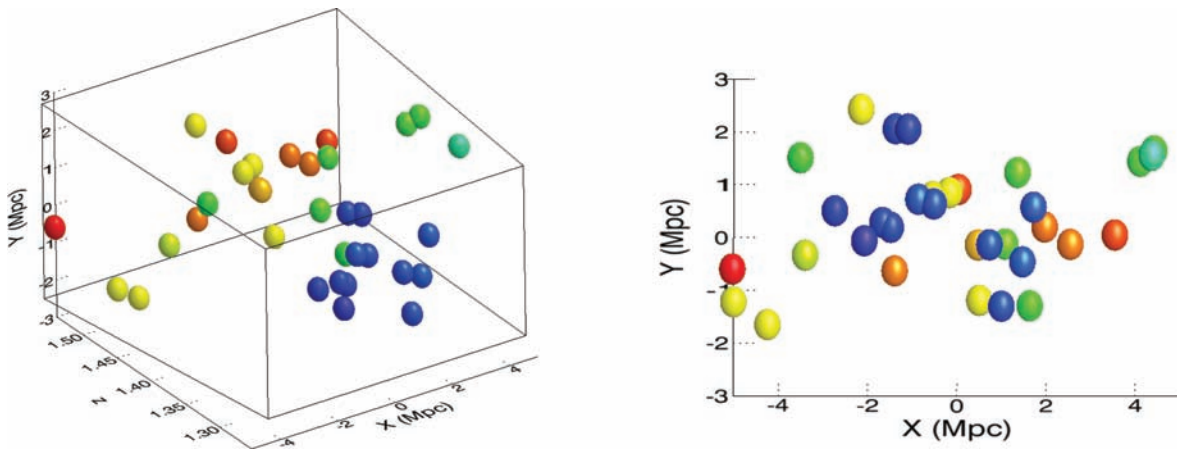


Figure 4. The three-dimensional distribution of galaxies within our spectroscopic sample (see Fig. 2: red circles) in comoving coordinates (X corresponds to RA, Y corresponds to Dec. and z corresponds to redshift). The plotted box reflects the field of CVB13 as defined in Section 2.3; the front and back faces are defined by the RA and Dec. limits as described in the caption of Fig. 1. The galaxies are colour-coded to redshift, from blue at $z = 1.25$ to red at $z = 1.53$. Right-hand panel: XY -projection of the galaxy distribution.

Table 1. Properties of the [O II] emitters.

ID	RA (h m s)	Dec. (° ′ ″)	z_{spec}	$F_{[\text{O II}]}$ ($10^{-20} \text{ W m}^{-2}$)	$L_{[\text{O II}]}$ (10^{34} W)	EW_0 (Å)	SFR ($\text{M}_{\odot} \text{ yr}^{-1}$)	i'	L_K (L_K^*)
CVB13_1	02:18:04.411	-05:01:08.25	1.254 27	4.8	4.4 ± 0.4	17	6.2 ± 1.8	22.480	3.5
CVB13_2	02:18:07.815	-04:59:17.22	1.267 12	1.0	1.0 ± 0.4	25	1.3 ± 0.7	23.777	1.1
CVB13_3	02:18:06.449	-05:00:54.87	1.274 53	1.2	1.1 ± 0.4	11	1.5 ± 0.7	23.292	2.1
CVB13_4	02:18:05.804	-05:00:50.10	1.275 80	2.3	2.2 ± 0.4	16	3.1 ± 1.0	22.934	1.7
CVB13_5	02:18:06.826	-04:59:17.36	1.276 05	2.8	2.7 ± 0.4	17	3.8 ± 1.2	23.772	1.8
CVB13_6	02:18:09.768	-05:00:31.80	1.281 99	1.1	1.0 ± 0.1	11	1.5 ± 0.4	24.226	0.2
CVB13_7	02:18:15.069	-05:02:12.49	1.283 38	2.5	2.4 ± 0.1	19	3.3 ± 1.0	22.693	1.3
CVB13_8	02:18:14.116	-05:01:12.02	1.283 50	2.2	2.1 ± 0.1	23	3.0 ± 0.9	24.588	0.3
CVB13_9	02:18:08.568	-05:00:27.32	1.285 17	10.1	9.9 ± 0.1	51	13.8 ± 4.0	23.610	0.3
CVB13_10	02:18:17.524	-05:00:34.91	1.286 29	9.8	9.6 ± 0.1	20	13.4 ± 3.8	22.642	2.7
CVB13_11	02:18:16.661	-05:01:28.73	1.286 76	1.5	1.5 ± 0.1	48	2.1 ± 0.6	26.278	0.5
CVB13_12	02:18:16.402	-05:02:08.13	1.400 24	1.3	1.5 ± 0.5	18	2.1 ± 0.9	23.027	1.5
CVB13_13	02:18:25.450	-04:59:44.17	1.405 08	1.5	1.8 ± 0.5	11	2.6 ± 1.0	23.371	3.1
CVB13_14	02:18:24.377	-04:59:54.12	1.411 19	3.5	4.2 ± 0.1	46	5.9 ± 1.7	22.753	0.7
CVB13_15	02:18:15.406	-05:00:04.62	1.411 20	5.6	6.9 ± 0.1	69	9.6 ± 2.8	24.243	0.2
CVB13_16	02:18:14.512	-05:01:10.79	1.411 48	4.0	5.0 ± 0.1	38	6.9 ± 2.0	23.489	0.9
CVB13_17	02:17:59.932	-05:01:20.99	1.444 05	4.3	5.6 ± 0.1	39	7.9 ± 2.3	23.875	0.8
CVB13_18	02:17:54.806	-05:02:03.29	1.453 19	3.6	4.7 ± 0.1	87	6.6 ± 1.9	24.173	0.6
CVB13_19	02:18:12.424	-05:02:01.65	1.453 31	7.4	9.7 ± 0.1	23	13.6 ± 3.9	23.012	3.4
CVB13_20 ^a	02:17:57.251	-05:02:23.82	1.453 49	1.6	2.1 ± 0.1	62	2.9 ± 0.8	23.484	3.9
CVB13_21	02:18:09.084	-05:00:27.58	1.453 93	1.1	1.5 ± 0.1	11	2.1 ± 0.6	23.398	0.5
CVB13_22	02:18:03.930	-04:59:08.76	1.454 79	4.2	5.5 ± 0.1	29	7.7 ± 2.2	23.600	1.0
CVB13_23	02:18:10.251	-05:00:24.12	1.455 58	1.9	2.5 ± 0.1	23	3.4 ± 1.0	24.448	0.4
CVB13_24A	02:18:12.252	-05:01:11.44	1.469 68	8.2	1.1 ± 0.1	91	15.5 ± 4.4	23.134	0.8
CVB13_24B	02:18:12.172	-05:01:11.65	1.472 74	5.0	6.8 ± 0.1	43	9.5 ± 2.7	23.134	$\lesssim 0.3$
CVB13_25	02:18:06.292	-05:01:34.62	1.484 64	5.7	7.9 ± 0.1	85	11.1 ± 3.2	23.606	1.1
CVB13_26	02:18:18.700	-05:01:10.74	1.484 72	3.2	4.4 ± 0.1	43	6.2 ± 1.8	24.398	0.4
CVB13_27	02:18:16.859	-05:00:55.27	1.488 96	4.0	5.6 ± 0.1	24	7.9 ± 2.3	23.809	2.3
CVB13_28	02:18:10.725	-05:00:22.11	1.499 51	7.4	1.1 ± 0.1	57	14.6 ± 4.2	23.910	0.4
CVB13_29	02:18:21.719	-05:01:02.32	1.501 86	3.3	4.7 ± 0.6	58	6.5 ± 2.0	24.033	1.4
CVB13_30	02:17:54.986	-05:01:32.49	1.539 05	5.8	8.9 ± 0.6	29	12.4 ± 3.6	23.591	0.4

Notes. Column 1 states the galaxy ID; 24B was discovered serendipitously in the slit of 24A and does not meet the K limit of the parent sample. The RA and Dec. given in columns 2 and 3 are in equinox J2000. The (heliocentric) redshift and line flux of the emitters (columns 4 and 5) are derived from a double Gaussian fit to the [O II] 3727-Å line profile. The line luminosity is shown in column 6, and column 7 is the rest-frame equivalent width. Column 8 shows the SFR derived from $L_{[\text{O II}]}$ (following Kennicutt 1998) and column 9 is the i' -band magnitude (Vega). Column 10 shows the K -band luminosity in units of L_K^* at the galaxy's redshift, calculated with $M_K^* = -24.34$ (Lin et al. 2004) at $z = 0$ and assuming passive evolution (following prescriptions of BruzualCharlot 2003) with a formation redshift of $z_{\text{form}} = 4$. The error on the flux measurement is $\sim 1 \times 10^{-21} \text{ W m}^{-2}$, although in regions dominated by sky lines ($1.25 \lesssim z \lesssim 1.28$, $1.37 \lesssim z \lesssim 1.41$ and $z \gtrsim 1.5$) the error is on average four times higher. The error on the redshift measurement is estimated at 5×10^{-5} . The error on the luminosity is the propagated flux error. The error quoted for the SFR is the error derived from equation (1) and the error on the luminosity added in quadrature. ^aObserved with GMOS (see Van Breukelen et al., in preparation).

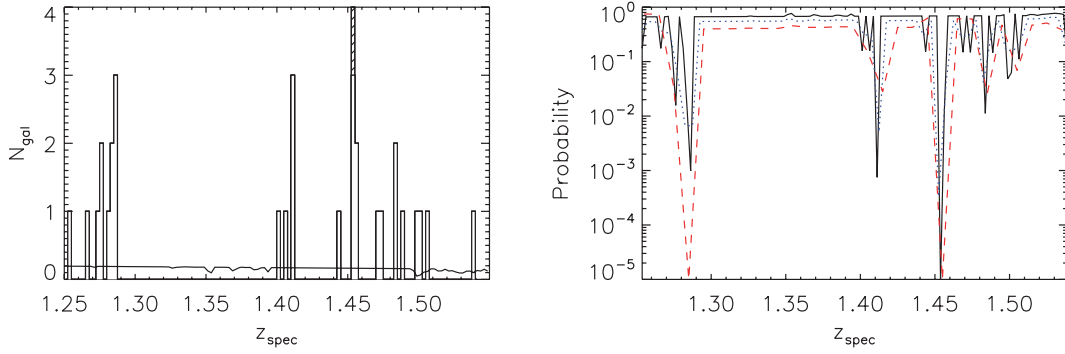


Figure 5. Left-hand panel: histogram of the spectroscopic redshifts of the targeted galaxies with detected [O II] emission in the field of CVB13. The shaded bin represents the galaxy observed with GMOS. Overplotted is the expected number of [O II] emitters per redshift bin, taking into account our detection completeness (see Section 3.2). The effects of the sky lines are somewhat smoothed in the plot owing to the binning of the histogram. Right-hand panel: the probability of the detected number of [O II] emitters per redshift bin being due to the background model, using the method of Brand et al. (2003) described in Section 3.3. The solid black line is for a bin size of $\Delta z = 0.0025$, the dotted blue line for $\Delta z = 0.005$, and the dashed red line for $\Delta z = 0.01$.

Other peaks in the redshift distribution could reflect genuine structures but could alternatively be due to Poisson noise in the background distribution. Note that if the completeness factor of point (i) in Section 3.2 is smaller than 0.25, the overdensities would be even more significant; if the factor is larger than 0.25 this would reduce the probability of the two structures up to ~ 0.01 for a factor of 1. However, this large a completeness value is disproved by the existence of the object CVB13'24B which has strong [O II] emission but $K > 20.6$, and by the occurrence of similar high equivalent width objects in the sample of Hogg et al. (1998).

We do not detect any obvious signs of clustering in RA and Dec. in our spectroscopic sample (see Fig. 4). This is principally because (i) we were unable to spectroscopically observe every photometric candidate cluster galaxy within the allocated time; (ii) the MOS instrument was unable to completely sample the cluster core, as slitlets cannot be placed within 1.5 arcsec along the spatial axis, nor next to each other along the dispersion axis as the spectra will overlap; and (iii) we could only determine redshifts for [O II] emitting galaxies and not for the red, passively evolving galaxies, which are customarily more clustered (e.g. Meneux et al. 2006).

3.4 Velocity dispersions and mass estimates

The line-of-sight velocity distribution of the two statistically robust structures at $z = 1.28$ and 1.45 is shown in Fig. 6. The biweighted mean of the redshifts and the ‘gapper’ estimate of the velocity dis-

persion are calculated for each of the structures, using the procedure outlined in Beers, Flynn & Gebhardt (1990). Subsequently, we estimate the masses of the groups using the relation between cluster mass M_{200} (the mass contained within a sphere of radius r_{200} for which the mean density is $200\rho_{\text{cr}}$) and virial velocity found by Evrard (2007):

$$M_{200} = \frac{10^{15} h^{-1} M_{\odot}}{H/H_0} \left(\frac{\sigma_{v,\text{los}}}{1080 \text{ km s}^{-1}} \right)^3, \quad (2)$$

where for a flat Universe

$$H(z) = H_0 \sqrt{\Omega_{\Lambda} + \Omega_M(1+z)^3}. \quad (3)$$

An alternative mass estimate is based on the stellar light of the groups observed in the K band. This is done in a number of steps. First, we calculate the K -band luminosity of each galaxy in terms of L_K^* at the appropriate redshift. This parameter is determined by assuming $M_K^* = -24.34$ for the cluster luminosity function (Lin, Mohr & Stanford 2004) at $z = 0$, and passive evolution of the K -band luminosity function, given a formation redshift of $z_{\text{form}} = 4$. Next, we sum all the luminosities of the observed galaxies and correct for the missed fraction of light due to the flux limit, according to the luminosity function of Lin et al. (2004). To arrive at the total mass, we then take a mass-to-light ratio $(M/M_{\odot})/(L/L_{\odot})$ of 75h (Rines et al. 2001) which is assumed constant with redshift *in terms of* L_K^* (note that assuming passive evolution of the luminosity function implies that L_K^* itself increases with redshift). The mass thus

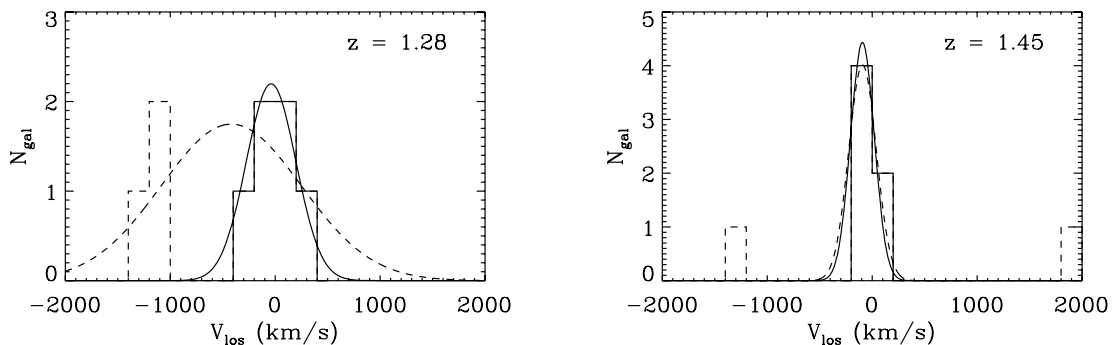


Figure 6. Left-hand panel: the line-of-sight velocity distribution for the structure at $z = 1.28$. The solid lines in both the histogram and the fitted Gaussian comprise all galaxies within a range of $\pm 1000 \text{ km s}^{-1}$ from the centre. The dashed lines show the sample within $\pm 2000 \text{ km s}^{-1}$. Right-hand panel: velocity distribution for the structure at $z = 1.45$. Line styles are as in the diagram in the left-hand panel.

estimated is only a lower limit, as we do not correct for the fact that our spectroscopic sampling of the group members is most likely incomplete.

As is illustrated in Fig. 6 (left-hand panel), the mean redshift and velocity dispersion of the structure at $z = 1.28$ are highly dependent on the limit imposed on the individual galaxy velocity for group membership. If we assume that all galaxies within a range of 2000 km s^{-1} are members of the group, we obtain a mean redshift of $\bar{z} = 1.282 \pm 0.002$ and a velocity dispersion of $\sigma_{v,\text{los}} = 668 \pm 149 \text{ km s}^{-1}$. Placing the limit at 1000 km s^{-1} , however, gives $\bar{z} = 1.2847 \pm 0.0008$, $\sigma_{v,\text{los}} = 236 \pm 63 \text{ km s}^{-1}$. Assuming that the group is virialized, the dynamically inferred masses are 5×10^{14} and $3 \times 10^{13} M_{\odot}$, respectively. The mass estimates from the total stellar light are 8×10^{13} and $4 \times 10^{13} M_{\odot}$, respectively, for the two galaxy samples.

The structure at $z = 1.45$ gives similar velocity distributions for the samples in the two velocity ranges (see Fig. 6, right-hand panel). We arrive at $\bar{z} = 1.4542 \pm 0.0004$ and $\sigma_{v,\text{los}} = 113 \pm 57 \text{ km s}^{-1}$; the inferred dynamical mass is only $5 \times 10^{12} M_{\odot}$. The mass derived from the stellar light yields a much higher estimate of $9 \times 10^{13} M_{\odot}$. Since we have spectroscopic confirmation for six to eight galaxies in the group with a total stellar mass of $1.6\text{--}1.8 \times 10^{12} M_{\odot}$, we believe that approximately a few $10^{13} M_{\odot}$ is a sensible minimum mass for the associated dark matter halo.

3.5 X-ray and radio properties

We have performed an analysis of the X-ray emission around CVB13. Fig. 7 (left-hand panel) shows a three-colour ($Bi'K$) image of the central 3×3 -arcmin² field with X-ray and radio (VLA B array) contours overlaid. We detect X-ray emission at RA = $02^{\text{h}}18^{\text{m}}09^{\text{s}}$ and Dec. = $-05^{\circ}00'30''$ (object X2, see Table 2 and Ueda et al., in preparation, source no. 0712) which is coincident with the optical/near-infrared cluster position. The X-ray source appears extended with a deconvolved size of ~ 5 arcsec (the *XMM* point

spread function is ~ 6 arcsec). The total X-ray flux is $F_X = 9.1 \times 10^{-18} \text{ W m}^{-2}$, which would mean a luminosity of $L_X = 8.9 \times 10^{36} \text{ W}$ if the emission is associated with the cluster at $z = 1.28$ or $L_X = 1.2 \times 10^{37} \text{ W}$ at $z = 1.45$. This would be indicative of a cluster mass of $\sim 10^{14} M_{\odot}$ for one of the clusters, or $\sim 8 \times 10^{13} M_{\odot}$ each if both clusters contribute equally to the X-ray flux (Reiprich & Böhringer 2002). The signal-to-noise ratio is too low to allow us to detect the 6.4-keV iron line and thus we cannot assign a secure redshift to the X-ray source. However, enough photons are detected in the source to conduct a crude hardness ratio (HR) spectral analysis. The HR values are $\text{HR2} = (C_3 - C_2)/(C_2 + C_3) = 0.38 \pm 0.22$ and $\text{HR3} = (C_4 - C_3)/(C_3 + C_2) = 0.01 \pm 0.16$, where C_2 is the 0.5–2.0 keV count rate, C_3 the 2.0–4.5 keV count rate, and C_4 the 4.5–10.0 keV count rate (Ueda et al., in preparation). These ratios mean that the X-ray spectrum is much harder than typical for a cluster, and is more characteristic for an absorbed AGN (e.g. Della Ceca et al. 2004). However, we do not find evidence for a single obscured AGN (e.g. a 24- μm or radio source) at the exact position of the X-ray emission. This is a puzzling system which is at face value an extended hard X-ray source. It requires an emission mechanism beyond any simple addition of a single obscured, non-thermal AGN and thermal cluster emission. Two such mechanisms that can cause the extended hard X-ray emission are inverse Compton scattering (see e.g. Fabian et al. 2006b) or confusion of more than one hard-spectrum X-ray source.

There is a significantly brighter X-ray source ~ 40 arcsec to the south-west of CVB13 (X1, see Fig. 7, left-hand panel). It is uncertain if it is physically associated with the weaker extended X-ray emission; however, it is certainly associated with a distant galaxy. A third X-ray source in the field (X3) is associated with an AGN at a redshift coincident with the $z = 1.28$ structure (see Table 2). Table 2 also shows the properties of the eight brightest radio sources in the field shown in Fig. 7 (left-hand panel). There are radio sources associated with both the $z = 1.28$ and the $z = 1.45$ clusters, but the bright radio source RB4 closest to CVB13 is associated with a foreground galaxy at $z \sim 0.5$. In Fig. 7 (right-hand panel), we plot a

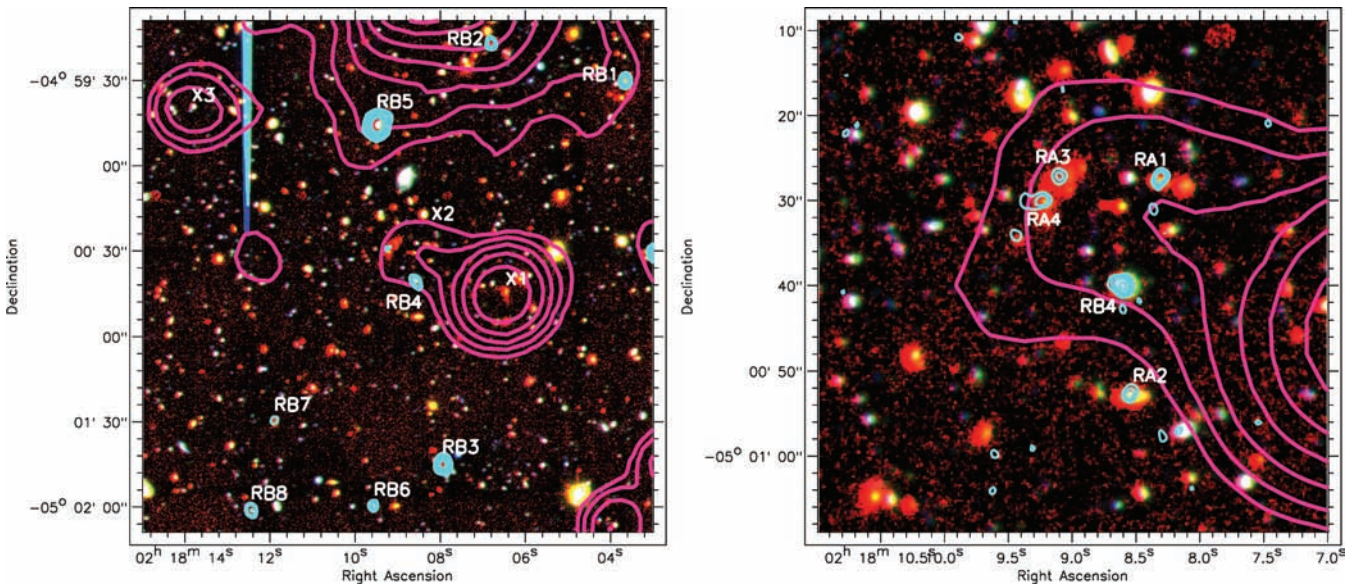


Figure 7. Left-hand panel: $Bi'K$ colour image (Furusawa et al., in preparation) of the central 3×3 -arcmin² region of CVB13. X-ray contours are from a signal-to-noise ratio radio map in the 0.5–2 keV band and are overlaid in purple [contour levels at $(\sqrt{2}\sigma, 2\sigma, 2\sqrt{2}\sigma, \dots)$]; the 1.4-GHz VLA B-array radio map is contoured in blue [contour levels at $(4\sigma, 4\sqrt{2}\sigma, 8\sigma, \dots)$]. The radio beam size is $5 \times 4 \text{ arcsec}^2$ at PA = 170° . X-ray and radio sources are labelled as in Table 2. Right-hand panel: colour image as in the left-hand panel, zoomed in on the central 1×1 -arcmin² region. The radio contours are from the higher resolution VLA A-array radio map [contour levels at $(2\sqrt{2}\sigma, 4\sigma, 4\sqrt{2}\sigma, \dots)$], with a beam size of $1.9 \times 1.6 \text{ arcsec}^2$ at PA = 22° .

Table 2. Table of the X-ray and radio sources in the 3×3 -arcmin² central region of CVB13.

ID	RA (^h ^m ^s)	Dec. ([°] ['] ^{''})	F (W m ⁻²)	z_{photo}	z_{spec}	Reference
X1	02:18:06.52	−05:00:43.9	$2.5 \pm 0.3 \times 10^{-17}$	1.06	–	
X2	02:18:08.37	−05:00:30.3	$9.1 \pm 2.1 \times 10^{-18}$	–	–	
X3	02:18:13.83	−04:59:39.2	$6.4 \pm 1.5 \times 10^{-18}$	–	1.258	Simpson et al. (in preparation)
	(^h ^m ^s)	([°] ['] ^{''})	(μJy)			
RB1	02:18:03.66	−04:59:30.1	122 ± 26	1.05	–	
RB2 ^a	02:18:06.83	−04:59:16.8	174 ± 50	1.11	1.276	This paper (CVB13_5)
RB3	02:18:07.94	−05:01:45.0	256 ± 27	–	–	
RB4	02:18:08.59	−05:00:40.0	102 ± 29	–	0.493	Simpson (private communication)
RB5	02:18:09.48	−04:59:45.5	2347 ± 28	1.35	1.094	Simpson et al. (in preparation)
RB6	02:18:09.55	−05:02:00.0	68 ± 22	–	1.268	Simpson (private communication)
RB7	02:18:11.89	−05:01:29.6	49 ± 21	0.75	0.918	This paper
RB8	02:18:12.44	−05:02:01.3	104 ± 27	1.32	1.453	This paper (CVB13_19)
RA1	02:18:08.30	−05:00:27.2	67 ± 20	1.02	–	
RA2	02:18:08.57	−05:00:52.8	73 ± 30	0.94	–	
RA3	02:18:09.10	−05:00:27.2	66 ± 29	1.27	1.454	This paper (CVB13_21)
RA4	02:18:09.23	−05:00:30.0	109 ± 38	1.32	–	

Notes. The IDs correspond to the labels in Fig. 7. The RA and Dec. are given in columns 2 and 3. The values in column 4 are the X-ray flux (0.5–10 keV) for the X-ray sources, and the 1.4-GHz radio flux density for the radio sources. The photometric redshifts (column 5) were determined as described in VB06. The spectroscopic redshifts (column 6) are from various sources as referenced in column 7.

^aThis object appears to be a resolved source in the B-array data, but the A-array data show that it actually consists of three separate objects. The central object on its own has a flux of $F = 113 \pm 24 \mu\text{Jy}$.

zoomed-in view of the CVB13 field and overplot the contours of the VLA A configuration map. This confirms four weak radio sources tentatively seen in the B-configuration map (Fig. 7, left-hand panel). One of these objects (RA3) has spectroscopically been confirmed to be at $z = 1.45$. RA4 has similar colours and photometric redshift and is therefore likely to be part of the same cluster. There is inconclusive evidence that the radio source associated with this galaxy has the ‘head–tail’ structure characteristic of galaxies moving with respect to an ICM.

If the radio emission is solely due to synchrotron radiation from a starburst, the SFR of a radio source with a 1.4-GHz flux density of $100 \mu\text{Jy}$ is $\sim 1400 M_{\odot} \text{yr}^{-1}$ in stars with masses of $> 5 M_{\odot}$ (see Condon 1992). Assuming a Salpeter IMF, this would mean an SFR ($M > 0.1 M_{\odot}$) of $\sim 7000 M_{\odot} \text{yr}^{-1}$. The SFR derived from the [O II] emission of these objects is only $\sim 10 M_{\odot} \text{yr}^{-1}$, and although this estimate does not take extinction into account and is therefore a lower limit, the submillimetre SCUBA Half Degree Extragalactic Survey (SHADES, e.g. Coppin et al. 2006) covers this region and does not identify any highly obscured starbursts. If, on the other hand, all radio emission is ascribed to AGN activity, we would expect (using Simpson et al. 2006, equation 9) a total X-ray luminosity of $\sim 10^{-16} \text{W m}^{-2}$ in the 2–10 keV range. The object X2 only has a flux in this band of $\sim 10^{-17} \text{W m}^{-2}$; therefore, confusion between hard X-ray sources associated with the radio sources is a possible explanation for this seemingly extended hard X-ray source.

4 CONCLUDING REMARKS

We have obtained multiobject spectroscopy on a photometrically selected cluster candidate at $z = 1.4$. Instead of a single massive cluster, we find three projected structures of galaxies at $z = 1.40$, 1.45 and 1.48, one of which (at $z = 1.45$) is statistically robust. We also serendipitously detect a robust structure at $z = 1.28$. Both the

structure at $z = 1.45$ and the one at $z = 1.28$ have masses $\sim 10^{14} M_{\odot}$ and may therefore be termed poor galaxy clusters.

The evolutionary status of both the $z = 1.28$ and the $z = 1.45$ clusters is uncertain. The cluster at $z = 1.45$ has a significantly lower virial mass than its mass derived from the total observed luminosity. It is very likely that this structure is not yet virialized, which would suppress the derived (three-dimensional) velocity dispersion of $\sim 200 \text{km s}^{-1}$. The velocity shear (half-width to zero intensity) observed in CVB13'21 – located centrally within the cluster – is 320km s^{-1} , which shows that the measured velocity dispersion of the cluster is unlikely to represent the total cluster mass. Note, however, that low-number statistics make an accurate determination of the velocity dispersion unfeasible. The total measured SFRs are ~ 45 and $\sim 60 M_{\odot} \text{yr}^{-1}$, respectively, for the clusters at $z = 1.28$ and 1.45, which for a mass of $\sim 1 \times 10^{14} M_{\odot}$ within $4 \times 4 \times 4 \text{Mpc}^3$ (co-moving) is a factor of 3–5 higher than typical SFRs observed in the field at these redshifts (e.g. Conolly et al. 1997).

The analysis of the cluster galaxies in this paper is based solely on redshifts estimated from [O II] emission-line features. Therefore, the overdensities we find at $z = 1.28$ and 1.45 only consist of star-forming galaxies, whereas the candidate cluster found by VB06 was selected with a photometric redshift algorithm which is sensitive to red, passively evolving galaxies. Out of the 18 highest-priority targets of sample 1, 10 were observed, and only six redshifts were obtained, two of which were confirmed to be cluster members. The other galaxies were all priority 3 targets of sample 1. We suspect that there will be an appreciable number of red galaxies in the cluster that we were unable to confirm spectroscopically. More observations of the central cluster galaxies, specifically for the cluster at $z = 1.45$, may also produce a higher velocity dispersion measurement. To thoroughly understand the nature and masses of the structures, we need to be able to obtain redshifts for this type of galaxy as well. Deep, near-infrared spectroscopy, for example, with the Fibre Multi Object Spectrograph (FMOS, Dalton et al. 2006), will give a more

complete sample and therefore yield a more comprehensive result for high-redshift galaxy clusters.

The extended X-ray luminosity at the position of these structures is characteristic of a cluster with a mass of $\sim 10^{14} M_{\odot}$. However, the X-ray spectrum is too hard to be simply caused by thermal cluster gas emission. A non-thermal effect like inverse Compton scattering could cause an X-ray detection with a spectral shape reflecting the energy distribution of the underlying electron population. The most likely explanation, however, is confusion caused by more than one AGN contributing to the X-ray emission. To shed light on the exact nature of this system, it will be interesting to study the cluster gas via the S-Z effect and the dark matter mass via lensing.

The original mass estimate of CVB13 by VB06 of $3 \times 10^{14} M_{\odot}$ is likely to be overestimated due to the superposition of the two lower mass structures at $z = 1.40$ and 1.48 . The single structure at $z = 1.28$ contains too few galaxies to be isolated by the same selection algorithm. This result suggests that spectroscopic follow-up is a vital element of photometric cluster surveys as the latter are prone to projection effects and can seriously overestimate cluster masses. To determine the impact of these effects, we calculate the probability of finding three groups in projection within $\Delta z = 0.1$ in a survey such as the one presented in VB06. Assuming a Sheth-Tormen cluster mass function (Sheth & Tormen 1999), we expect to find 121 groups with masses of a few $10^{13} M_{\odot}$ and six clusters with masses of $\sim 10^{14} M_{\odot}$ within the redshift range $1.25 \leq z \leq 1.55$ in a field of 0.5 deg^2 . Neglecting spatial clustering of the groups, there are on average two superpositions of three groups with masses $\sim 10^{13} M_{\odot}$ within a box of $2 \times 2 \text{ Mpc}^2$ and $\Delta z = 0.1$. The probability of finding a projection of two groups and one cluster of $\sim 10^{14} M_{\odot}$ (as for CVB13) is 45 per cent. Running the cluster algorithm of VB06 on a simulated superposition of three groups shows that in order to distinguish between massive clusters at this redshift and projected groups with a redshift separation of $\Delta z = 0.05$, the photometric redshift error needs to be as small as $\frac{\sigma_z}{1+z} = 0.005$. The COMBO-17 survey (Wolf et al. 2004), which determined photometric redshifts from photometry in 17 bands, obtained a best redshift error of $\frac{\sigma_z}{1+z} = 0.01$ for galaxies with $R < 21$ (cf. $R \sim 24$ for CVB13 targets). Thus, attaining the order of accuracy needed in photometric redshifts to determine the cluster mass function at high redshifts seems very challenging, and we caution against attempting this with photometric techniques alone.

ACKNOWLEDGMENTS

The authors are grateful to Lance Miller for sharing his cluster mass function code. CvB would like to thank Oxford Astrophysics for studentship funding and CvB, DB and CS acknowledge funding from the Science and Technology Facilities Council. The data presented herein were obtained at the W. M. Keck Observatory, which is operated as a scientific partnership among the California Institute of Technology, the University of California and the National Aeronautics and Space Administration. The observatory was made possible by the generous financial support of the W. M. Keck Foundation. The authors wish to recognize and acknowledge the very significant cultural role and reverence that the summit of Mauna Kea has always had within the indigenous Hawaiian community. We are most fortunate to have the opportunity to conduct observations from this mountain. The analysis pipeline used to reduce the DEIMOS data was developed at UC Berkeley with support from NSF grant AST-0071048.

REFERENCES

- Abell G. O., 1958, *ApJS*, 3, 211
 Abell G. O., Corwin H. G., Olowin R. P., 1989, *ApJS*, 70, 1
 Beers T. C., Flynn K., Gebhardt K., 1990, *AJ*, 100, 32
 Birkinshaw M., 1999, *Phys. Rep.* 310, 97
 Bower R. G., Lucey J. R., Ellis R. S., 1992, *MNRAS*, 254, 601
 Brand K., Rawlings S., Hill G. J., Lacy M., Mitchell E., Tufts J., 2003, *MNRAS*, 344, 283
 Bremer M. N. et al., 2006, *MNRAS*, 371, 1427
 Bruzual G., Charlot S., 2003, *MNRAS*, 344, 1000
 Carlstrom J. E., Joy M. K., Grego L., Holder G. P., Holzapfel W. L., Mohr J. J., Patel S., Reese E. D., 2000, *Phys. Scrip. Vol. T*, 85, 148
 Cirasuolo M. et al., 2007, *MNRAS*, 380, 585
 Cole S., 1991, *AJ*, 367, 45
 Condon J. J., 1992, *ARA&A*, 30, 575
 Conolly A. J., Szalay A. S., Dickinson M., Subbarao M. U., Brunner R. J., 1997, *ApJ*, 486, L11
 Coppin K. et al., 2006, *MNRAS*, 372, 1621
 Cotter G. et al., 2002, *MNRAS*, 331, 1
 Cowley D. J., Faber S., Hilyard D. F., James E., Osborne J., 1997, *SPIE*, 2871, 1107
 Dalton G. et al., 2006, *SPIE Vol.* 6269, 136
 Danese L., de Zotti G., di Tullio G., 1980, *A&A*, 82, 322
 Della Ceca R. et al., 2004, *A&A*, 428, 383
 Evrard A. E. et al., 2007, *ApJ*, in press (astro-ph/0702241)
 Fabian A. C., Celotti A., Erlund M. C., 2006a, *MNRAS*, 373L, 16
 Fabian A. C., Sanders J. S., Crawford C. S., Ettori S., 2006b, *MNRAS*, 341, 729
 Gladders M. D., Yee H. K. C., 2005, *ApJS*, 157, 1
 Gladders M. D., Lopez-Cruz O., Yee H. K. C., Kodama T., 1998, *ApJ*, 501, 571
 Goto et al., 2002, *AJ*, 123, 1807
 Heckman T. M., 2002, in Mulchaey J. S., Stocke J., eds, *ASP Conf. Ser. Vol. 254, Extragalactic Gas at Low Redshift*. Astron. Soc. Pac., San Francisco, p. 292
 Hogg D. W., Cohen J. G., Blandford R., Pahre M. A., 1998, *ApJ*, 504, 622
 Hook I., Jørgensen I., Allington-Smith J. R., Davies R. L., Metcalfe N., Murowinski R. G., Crampton D., 2004, *PASP*, 116, 425
 Ivison R. J. et al., 2007, *MNRAS*, 380, 199
 Jones M. E. et al., 2005, *MNRAS*, 357, 518
 Kennicutt R. C., 1998, *ARA&A*, 36, 189
 Kim R. S. J. et al., 2002, *AJ*, 123, 20
 Kneissl R., Jones M. E., Saunders R., Eke V. R., Lasenby A. N., Grainge K., Cotter G., 2001, *MNRAS*, 328, 783
 Lawrence A. et al., 2007, *MNRAS*, 379, 1599
 Lin Y.-T., Mohr J. J., Stanford S. A., 2004, *ApJ*, 610, 745
 Lobo C., Iovino A., Lazzati D., Chincarini G., 2000, *A&A*, 360, 896
 Lonsdale C. J. et al., 2005, *PASP*, 115, 897
 Ly C. et al., 2007, *ApJ*, 657, 738
 Meneux B. et al., 2006, *A&A*, 452, 387
 Miller C. J. et al., 2005, *AJ*, 130, 968
 Osterbrock D. E., 1967, *PASP*, 79, 523
 Pascarella S. M., Windhorst R. A., Driver S. P., Ostrander E. J., Keel W. C., 1996, *ApJ*, 456, L21
 Postman M., Lubin L. M., Gunn J. E., Oke J. B., Hoessel J. G., Schneider D. P., Christensen J. A., 1996, *AJ*, 111, 615
 Reiprich T. H., Böhringer H., 2002, *ApJ*, 567, 716
 Rines K., Geller M. J., Kurtz M. J., Diaferio A., Jarrett T. H., Huchra J. P., 2001, *ApJ*, 561, L41
 Rosati P. et al., 2004, *AJ*, 127, 230
 Röttgering H. J. A., West M. J., Miley G. K., Chambers K. C., 1996, *A&A*, 307, 376
 Scannapieco E., Oh S. P., 2004, *ApJ*, 608, 62
 Sheth R., Tormen G., 1999, *MNRAS*, 308, 119
 Simpson C. et al., 2006, *MNRAS*, 372, 741
 Stanford S. A., Bradford H., Rosati P., Tozzi P., Borgani S., Eisenhardt P. R., Spinrad H., 2001, *ApJ*, 552, 504

Stanford S. A. et al., 2006, ApJ, 646L, 13
Sunyaev R. A., Zeldovich Y. B., 1970, ASS, 7, 3
Sunyaev R. A., Zeldovich Y. B., 1972, Comments Astrophys., 4, 173
Van Breukelen C. et al., 2006, MNRAS, 373L, 26 (VB06)
Venemans B. et al., 2002, ApJ, 569L, 11

Watson M. G. et al, (the SXDS Collaboration), 2004, BAAS, 36, 1202
White S. D. M., Frenk C. S., 1991, AJ, 579, 16
Wolf C. et al., 2004, A&A, 421, 913

This paper has been typeset from a $\text{T}_{\text{E}}\text{X}/\text{L}_{\text{A}}\text{T}_{\text{E}}\text{X}$ file prepared by the author.